

JGR Atmospheres

RESEARCH ARTICLE

10.1029/2020JD033914

Key Points:

- The evolution of an AgI seeding track was documented by a combination of radar, satellite, and laser raindrop disdrometer observations
- The radar signature appeared 18 min after seeding, expanded at a rate of 1.4 m s^{-1} for 90 min while splitting into a double band
- A conceptual model of the evolution of the seeded clouds and precipitation is presented

Supporting Information:

Supporting Information may be found in the online version of this article.

Correspondence to:

Z. Yue, D. Rosenfeld, and L. Zhang,
Yue_zhiguo@163.com;
daniel.rosenfeld@huji.ac.il;
zhanglei@lzu.edu.cn

Citation:

Wang, J., Yue, Z., Rosenfeld, D., Zhang, L., Zhu, Y., Dai, J., et al. (2021). The evolution of an AgI cloud-seeding track in central China as seen by a combination of radar, satellite, and disdrometer observations. *Journal of Geophysical Research: Atmospheres*, 126, e2020JD033914. <https://doi.org/10.1029/2020JD033914>

Received 19 SEP 2020

Accepted 2 MAY 2021

Author Contributions:

Conceptualization: Zhiguo Yue, Daniel Rosenfeld
Data curation: Jin Wang
Formal analysis: Jin Wang, Zhiguo Yue, Daniel Rosenfeld
Funding acquisition: Lei Zhang, Yannian Zhu, Xing Yu, Jinhui Li
Methodology: Jin Wang, Zhiguo Yue, Daniel Rosenfeld, Xing Yu, Jinhui Li
Project Administration: Lei Zhang, Xing Yu, Jinhui Li
Software: Zhiguo Yue, Daniel Rosenfeld, Yannian Zhu, Jin Dai, Xing Yu, Jinhui Li
Supervision: Zhiguo Yue, Daniel Rosenfeld, Yannian Zhu

© 2021. American Geophysical Union. All Rights Reserved.

The Evolution of an AgI Cloud-Seeding Track in Central China as Seen by a Combination of Radar, Satellite, and Disdrometer Observations

Jin Wang^{1,2,3,4} , Zhiguo Yue^{2,4} , Daniel Rosenfeld⁵ , Lei Zhang^{1,6} , Yannian Zhu^{4,7} , Jin Dai^{4,7}, Xing Yu^{4,7}, and Jinhui Li^{2,4}

¹Key Laboratory for Semi-Arid Climate Change of the Ministry of Education, College of Atmospheric Sciences, Lanzhou University, Lanzhou, China, ²Center of Weather Modification of Shaanxi Province, Xi'an, China, ³Key Laboratory for Cloud Physics of China Meteorological Administration, Beijing, China, ⁴Key Laboratory of Eco-Environment and Meteorology for the Qinling Mountains and Loess Plateau, Xi'an, China, ⁵Institute of Earth Sciences, Hebrew University of Jerusalem, Jerusalem, Israel, ⁶Collaborative Innovation Center for Western Ecological Safety, Lanzhou University, Lanzhou, China, ⁷Meteorological Institute of Shaanxi Province, Xi'an, China

Abstract Operational cloud seeding has been implemented to alleviate local precipitation shortages in China for over half a century. Here, we present quantitative evidence for the effect of AgI seeding on supercooled layer clouds with a top cloud temperature of -15°C in China, as documented for the first time by a combination of radar, satellite, and disdrometer observations. A radar signature appeared 18 min after seeding, shortly followed by a visible glaciated seeding track. The seeding signature expanded horizontally at a rate of ~ 1.4 and $\sim 0.3 \text{ m s}^{-1}$ before and after 04:25 UTC. The radar signature descended to the surface 40 min after seeding. A disdrometer captured the precipitation of the first seeded raindrops that reached maximum diameter of 2.75 mm compared to the maximum diameter of 1 mm of the light background rain. The enhanced surface rainfall was observed within the subsequent 100 min. A conceptual model for the formation and expansion of the seeding track is presented. Although the precipitation was light, it is a promising step toward the goal of quantifying the impact of cloud seeding in China.

1. Introduction

In recent decades, many countries have performed scientific experiments on the enhancement of rainfall and/or snow volume. At the same time, many provinces in China have carried out operational precipitation enhancement to alleviate local precipitation shortages. Supercooled stratiform clouds are good targets for glaciogenic seeding in northern China during spring and autumn. When ice nuclei are seeded into clouds with abundant supercooled water, the conversion of supercooled water to ice is promoted, leading to an increase in precipitation efficiency and amount. This is the theoretical basis for artificially enhancing cold cloud precipitation.

When seeding materials are injected into the cloud top, the simplest and easiest-to-observe cloud-seeding feature is the glaciation and collapse of the cloud top (Langmuir, 1961), which indicates that the cloud-seeding materials have altered the microphysical characteristics and structure of the cloud. Radar is a common tool to identify microphysical changes in cloud properties resulting from cloud seeding (French et al., 2018; Friedrich et al., 2020; Geerts et al., 2010; Hobbs et al., 1981; Pokharel, Geerts, Jing, Friedrich, Aikins, et al., 2014). Based on measurements from ground-based X-band radars, an airborne W-band cloud radar and in situ physical cloud probes, French et al. (2018) provided strong evidence for the conclusion that initiation and growth of ice crystals results from winter orographic glaciogenic cloud seeding using silver iodide (AgI).

Satellite methodologies for cloud microphysics retrieval have also been applied to investigate the microphysical impact of cloud seeding and aerosol-cloud interactions (Rosenfeld, Zhu, et al., 2019; Yue et al., 2019). Rosenfeld (2000) used the advanced very high resolution radiometer (AVHRR) satellite data to study the impacts of urban pollution on cloud properties. Since 2000, the moderate-resolution imaging spectroradiometer (MODIS) has provided multiple cloud characteristics, including cloud phase, effective particle size, and cloud optical thickness (Platnick et al., 2017). Morrison et al. (2013) used these MODIS-retrieved cloud

Validation: Jin Wang, Zhiguo Yue, Daniel Rosenfeld, Yannian Zhu
Visualization: Jin Wang
Writing – original draft: Jin Wang
Writing – review & editing: Jin Wang, Zhiguo Yue, Daniel Rosenfeld, Yannian Zhu, Jin Dai

properties to identify regions of clouds containing supercooled liquid water with potential for glaciogenic cloud seeding. Satellite observations of glaciogenic cloud-seeding signatures were revealed by a conspicuous cloud track on an AVHRR image for the first time in 2005. The seeding track was produced by a seeding thick supercooled layer of clouds over central China. The seeding tracks were observed by the retrieval of cloud microphysical properties and supported by the simulated diffusion of seeding materials (Rosenfeld, Yu, & Dai, 2005; Yu et al., 2005). An aircraft AgI seeding experiment on supercooled water clouds in Eastern China was followed by in situ aircraft documentation of the formation of the ice hydrometeors. Concurrent Himarawi-8 satellite observations detected an increase in the cloud top brightness temperature caused by the falling of the ice particles and consequential collapse of the cloud top within the seeding track (Dong et al., 2020).

Rauber et al. (2019) noted that a deficiency in cloud-seeding evaluations remains ground validation of seeding effects in target experiments. Hobbs (1975) proposed the first physical evidence of the effectiveness of seeding material in orographic clouds when increased concentrations of silver in snow were detected. Super et al. (1988), Super and Boe (1988), and Huggins (2007) reported that ground-based AgI seeding has enhanced the ground precipitation rates (less than 1 mm h^{-1}) of stable orographic clouds. The project “AgI Seeding Cloud Impact Investigating” had 25 experimental units (Pokharel, Geerts, & Jing, 2018). A positive effect on the surface precipitation amounts was shown by the double ratio methodology (Pokharel, Geerts, Jing, Friedrich, Ikeda, & Rasmussen, 2017). Although the impacts of cloud seeding on season-long precipitation values have been estimated in many experiments (Gabriel, 1999; Manton et al., 2011; Rasmussen et al., 2018), there are two remaining issues in the verification of the impacts of seeding on ground precipitation. One is the matter of how to clearly identify the time and location of the seeded cloud in the natural cloud system; the other is the major challenge of accurately detecting increased surface precipitation (Flossmann et al., 2018). Gultepe et al. (2014) argued that extracting signals from cloud systems with a high natural variability presents a major obstacle for researchers. Friedrich et al. (2020) identified areas of orographic precipitation that were unambiguously generated by cloud seeding through the identification of seeding tracks with enhanced radar reflectivity, which could then be connected to enhanced surface snowfall.

Due to the advances in the performance of numerical models, numerical models are becoming an indispensable tool for the developing technologies related to the two aforementioned issues and the ability to assess cloud seedability in precipitation enhancement studies. Xue et al. (2013) found different effects between aircraft-based and ground-based seeding by using a two-dimensional version of the Weather Research and Forecasting model coupled with a cloud-seeding parameterization. Large eddy simulation models have been implemented in many studies to investigate the AgI seeding of orographic clouds (Chu et al., 2014, 2016, 2017; Xue et al., 2016). The results show that the vertical dispersion of the seeding material is a limitation of effective seeding and suggest that seeding does not significantly impact the dynamics of orographic clouds. While the numerical model simulations provide some evidence of the effects of AgI seeding, their validation in the real atmosphere is necessary.

For the case presented in this study, we focus on the effects of cloud seeding on supercooled stratiform clouds over central China on March 19, 2017. Our study is unique due to the following factors: (a) it combines radar, satellite, and disdrometer observations of the spatial and temporal evolution of seeded stratiform clouds, (b) the light precipitation generated by cloud seeding is isolated since there is very little natural background precipitation, (c) the raindrop spectra of the seeding-induced precipitation are observed for the first time, and (d) a conceptual model of the evolution of the seeded clouds and precipitation is presented. This study is divided into three parts. Section 2 briefly describes the operational cloud-seeding methods, implemented technologies, and atmospheric conditions. Sections 2.1–2.3 provide observations and analyses from radar, satellite retrieval, and surface precipitation, respectively. Section 3 generically summarizes the hypothesized chain of events and discusses relevant important issues.

2. Operational Seeding on March 19, 2017

In the Shaanxi Province, located at the center of China, operational cloud seeding has been carried out continuously every spring and autumn since 1978. The accompanying observational instruments have constantly improved. On March 19, 2017, operational cloud seeding was conducted in the region and covered

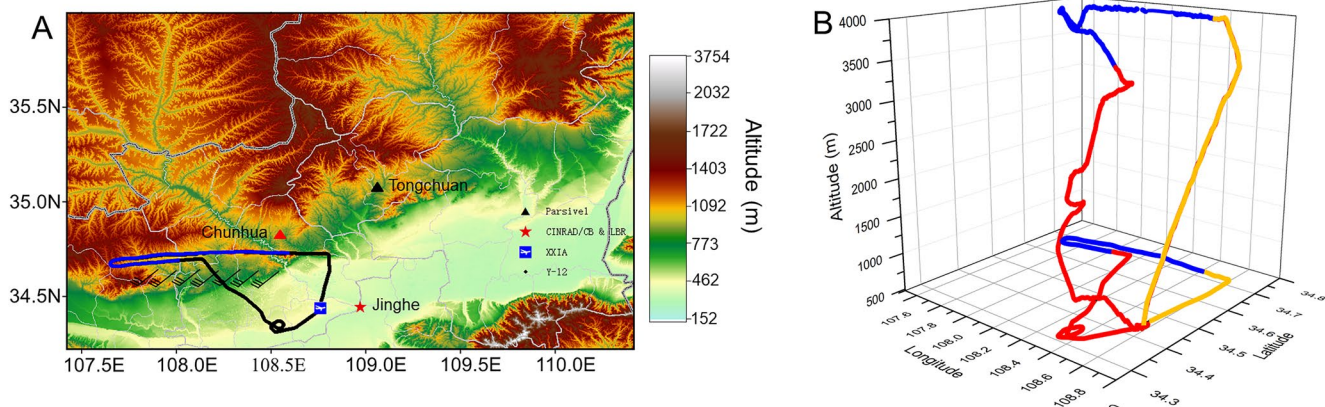


Figure 1. Topography, aircraft flight track, and observational instruments on the ground around the cloud-seeding region on March 19, 2017. (a) The triangles represent the particle size velocity (PARSIVEL) disdrometers located at the Chunhua (red) station (108.55°E, 34.83°N) and the Tongchuan (black) station (109.08°E, 35.06°N). Wind barbs plotted below the aircraft track illustrate the mean wind direction and speed (in meters per second) at a flight level of 3,944 m. A full barb equals 4 m s^{-1} . (b) Three-dimensional plot and ground projection of the flight path of the cloud-seeding aircraft. The solid blue line shows the seeded segment (02:41–03:14 UTC) of the flight track. The gold and red segments represent the ascending and descending stages, respectively.

parts of the Guanzhong Plain and the Loess Plateau (Figure 1a). The AgI aerosols were released by a YUN-12 transport aircraft (Y-12) equipped with a GPS.

The Y-12 aircraft took off from Xi'an-Xianyang Airport (the blue sign with an airplane symbol in Figure 1a) at 02:25 UTC and flew 33 km to the north (Figure 1a). The aircraft began cloud seeding after turning westward at 02:41 UTC. The average seeding altitude of the aircraft was 3,944 m during the period of 02:41–03:03 UTC with a horizontal flight distance of 97 km. At 03:04 UTC, the aircraft descended to 3,663 m and then climbed to approximately 3,900 m. The aircraft then reversed course and flew eastward at 03:06 UTC due to instruction from airspace control. From 03:06 UTC to 03:14 UTC, the flight altitude was at its lowest, averaging at 3,191 m (Figure 1b). The airborne cloud seeding lasted 34 min and terminated at 03:14 UTC. During the operation of the cloud-seeding aircraft, the AgI aerosols were released by burning 750 g of burn-in place pyrotechnic flares at a seeding rate of 0.368 g s^{-1} within an ambient temperature near -15°C (Figure 3).

The C-band China new generation weather radar (CINRAD/CB) and the L-band sounding radar were located at the Jinghe meteorological station (108.97°E, 34.45°N, 410 m above sea level, red star in Figure 1a). The height of the CINRAD/CB antenna from the ground was 48.6 m. CINRAD/CB operates for collecting rain measurements at 5,300–5,500 MHz (with a center operating frequency of $5,400 \pm 15 \text{ MHz}$) with a wavelength of 5.6 cm. The composite radar reflectivity products of CINRAD/CB from the Jinghe station in Xi'an, Shaanxi Province, are used in this study. Composite reflectivity is a product in which the largest reflectivity detected from constant elevation-azimuth scans within a volume scan has been projected onto a Cartesian grid point. The C-band radar had an antenna beam width of 1° , and it adopted the volume scan mode of nine elevation angles at 0.5° , 1.5° , 2.4° , 3.4° , 4.3° , 6.0° , 9.9° , 14.6° , and 19.5° . The radar completed one volume scan every 6 min. The radar data were quality controlled by filtering basic electromagnetic interferences, including interferences of land objects.

The L-band sounding data provided information on temperature, humidity, air pressure, wind direction, and wind speed. Soundings were launched twice at 00:00 UTC and 12:00 UTC every day. The real-time sounding data were only analyzed for physically implausible values, and those with gross errors were removed. Two particle size velocity (PARSIVEL) laser disdrometers were sited at the Chunhua (108.55°E, 34.83°N, and 1,013 m above sea level) and Tongchuan (109.08°E, 35.06°N, and 979 m above sea level) stations on the north (downwind) side of the seeding region (red and black triangles in Figure 1a). They continuously recorded the spectral characteristics of the rain with a sampling interval of 1 min. As long as precipitation particles passed through the laser beam ($3 \times 18 \text{ cm}$) of the PARSIVEL, their diameter and fall speed were recorded instantaneously (Löffler-Mang & Joss, 2000).

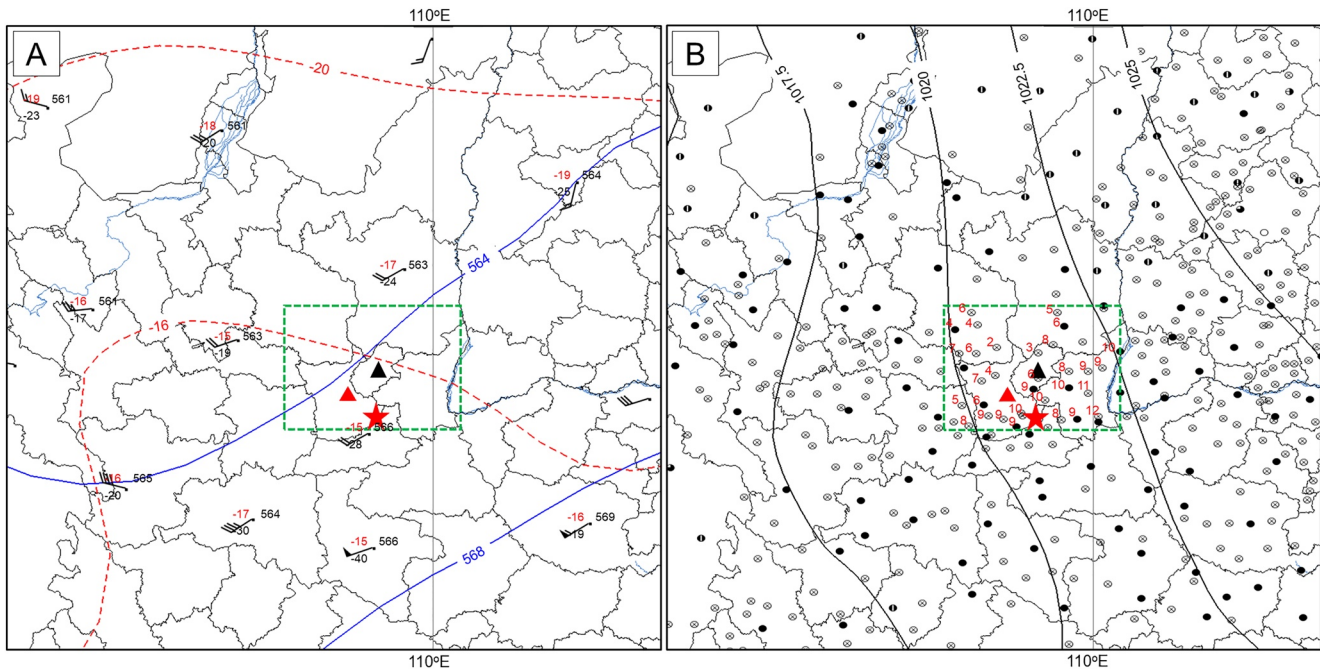


Figure 2. Synoptic conditions over the seeded area on March 19, 2017: (a) 500 hPa and (b) surface map for 00:00 UTC. The geopotential height lines (10 gpm, blue solid line, 40-gpm interval), isotherms (in degrees Celsius, red dotted line, 4° interval), surface temperature (red numbers), weather conditions (shown using the standard synoptic symbols), and sea level pressure (black solid line, 2.5 hPa) are shown here. The cloud-seeding region with two PARSIVEL stations (red and black triangles) and the Jinghe meteorological station (red star, 108.97°E, 34.45°N) is presented by the green dash-outlined region.

The primary synoptic system was an upper level trough and a warm ridge flank located over central China on March 19, 2017 (Figure 2a). Because the seeded region was located downstream of the tilted shortwave trough and the eastern flank of the upper trough, the horizontal warm advection was associated with the generally rising motion of the air in this part of the trough.

The surface temperature was greater than 0°C with a maximum of 12°C in the seeded region (Figure 2b). At 00:00 UTC, sporadic precipitation began falling to the west of the seeded area on the ground.

The sounding profile showed that the surface temperature at the Jinghe station (108.97°E, 34.45°N) was 9.7°C at 00:00 UTC. The altitudes of the 0°C, −4°C, and −8°C isotherms were 1,943, 2,682, and 3,944 m, respectively (Figure 3). The temperature of the cloud top derived from the sounding measurements was −10.6°C and −11.9°C as derived from the 11.2-μm brightness temperature (T_{11}) of the Himawari-8 satellite, which are in relatively good agreement. From 02:00 UTC to 06:00 UTC, the cloud top temperature was very homogenous near −15°C according to MODIS Terra. There was a strong temperature inversion layer present between 3,990 and 4,382 m.

The wind direction was southeast below 2.5 km and shifted southwest above 2.5 km. The wind speed increased with increasing altitude. The average wind speed was 12.3 m s^{−1} from 239° between 3,500 and 3,933 m (Figure 3). This mean wind speed and direction govern the transport of the seeding material but not the dispersion.

The relative humidity (RH) measurement of the sounding was saturated at 90%, indicating in-cloud passage. The vertical profile of the RH indicated that there was a single-layer cloud with a cloud base altitude near 1,500 m and a cloud top altitude of 4,100 m present at 00:00 UTC (Figure 3).

2.1. Evolution of Radar Echo

The evolution of the composite radar reflectivity (Figures 4a, 4c, 4e, 4g, and 4i) shows the radar composite reflectivity (i.e., the maximum reflectivity in the vertical direction) at 02:59, 03:16, 03:27, 04:47, and 05:49

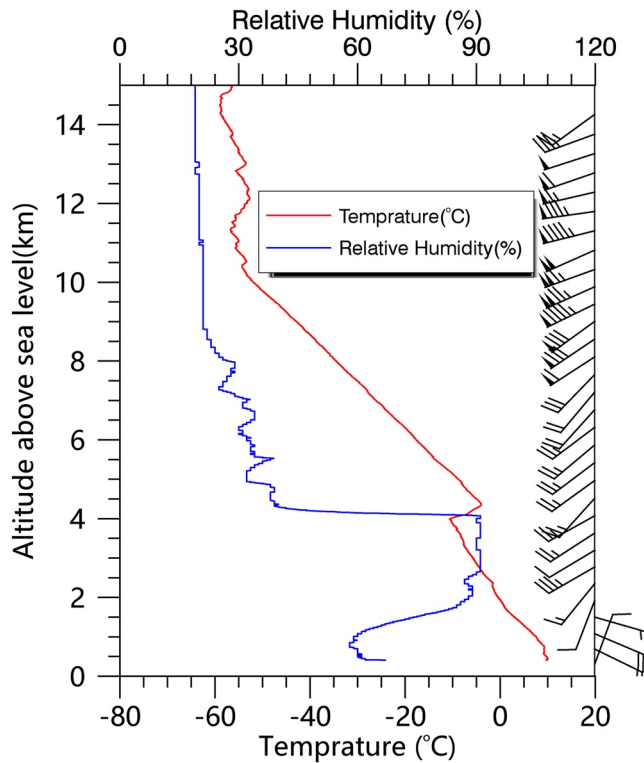


Figure 3. Temperature profile (red solid line), relative humidity profile (blue solid line), and wind speed and direction (black wind) determined from soundings at 00:00 UTC on March 19, 2017. The full barb equals 4 m s^{-1} , and the triangular flag equals 20 m s^{-1} .

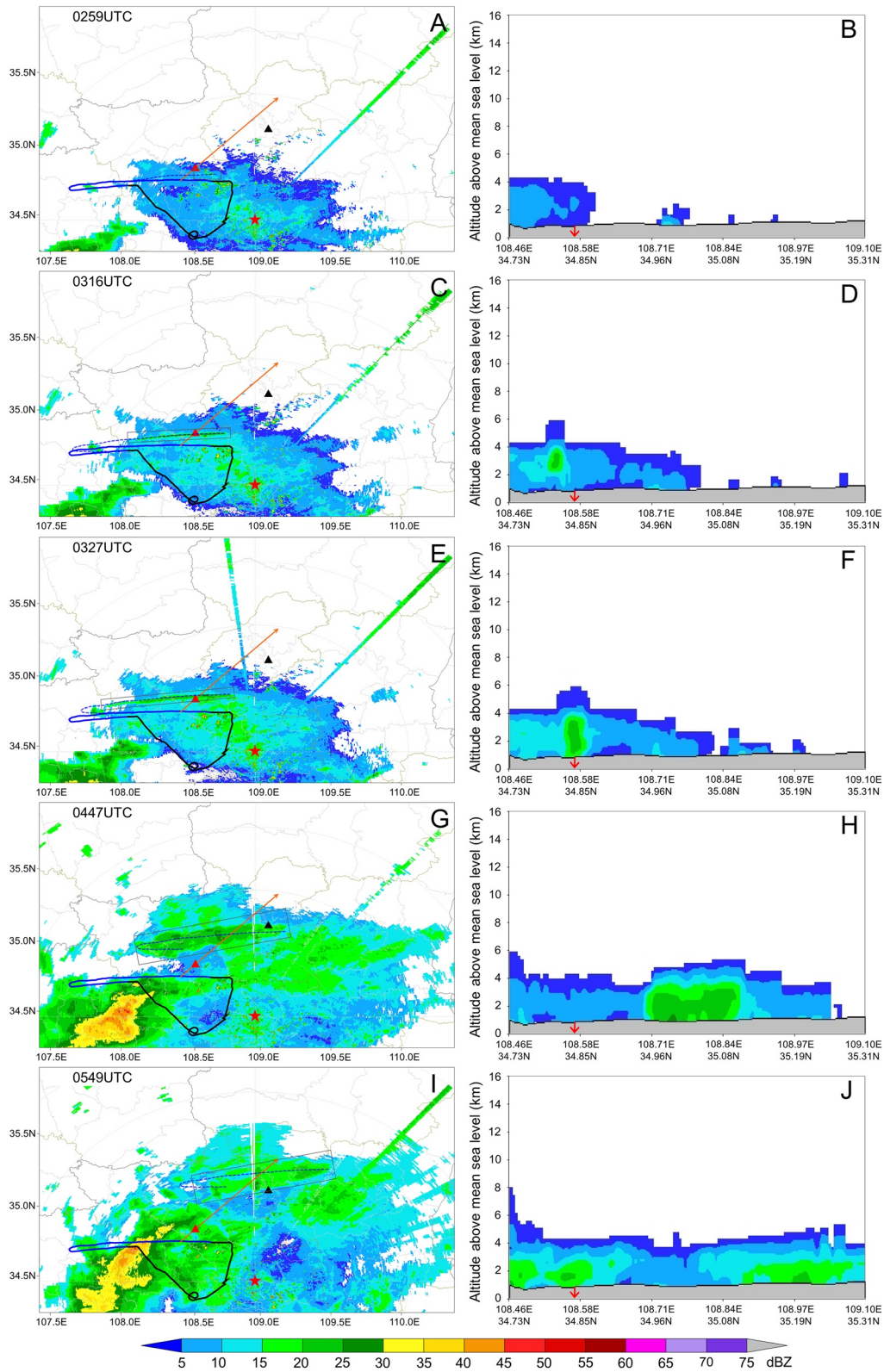
UTC, respectively. The maps of the composite radar reflectivity echo every 6 min from 02:36 UTC to 07:14 UTC are shown on the left panel in the additional Movie S1 and show that the seeding line was detectable for 234 min. It transitioned from the initial seeding line seen at the beginning of the period to a much larger and wider area of enhanced composite reflectivity as the seeding material dispersed. The seeding line marked with a gray rectangle first appeared at 02:59 UTC (Figure 4a); it was 13.4 km long and had an echo of 10–15 dBZ. The clear cloud-seeding signature started with an echo reflectivity of 10–15 dBZ on the downwind side of the aircraft flight trajectory. At 03:27 UTC (Figure 4e), the length and echo reflectivity of the line increased to 83.7 km and 25–30 dBZ, respectively. The width of the region of enhanced composite reflectivity greater than 15 dBZ exceeded 15 and 19 km at 04:47 UTC and 05:49 UTC (Figures 4g and 4i). The expansion rate, defined as one-half of the seeding line width in unit time, of the seeding line on the left panel in Movie S2, was 1.4 m s^{-1} and slowed to 0.3 m s^{-1} after 04:25 UTC (Figure 5). The seeding track split into a double peak band after 03:44 UTC. The maximum distance between the two reflectivity peaks greater than 20 dBZ was nearly 10 km (Figure 5). Under the prevailing southwest wind, the seeding line moved toward the northeast (from 239°) and gradually dissipated after moving 100 km after 3.5 h from the initial seeding time, near 06:35 UTC.

An investigation of the evolution of the radar seeding signature in the horizontal and vertical directions allowed us to better understand the microphysical changes within the seeded clouds. The vertical cross section of radar reflectivity along the orange solid line shown in Figure 4a, which is parallel to the wind direction, was used to track the vertical evolution of the seeding signature, in Figures 4b, 4d, 4f, 4g, and 4j. The full temporal resolution (6 min) of the horizontal and vertical radar seeding signatures is provided in Movie S1. The reflectivity of the seeded cloud increased

from the background values of approximately 10 dBZ to almost 30 dBZ. Before 02:59 UTC (Figure 4b), the radar reflectivity was less than 10 dBZ, reached 25–30 dBZ near the surface after 47 min and remained at that intensity for another 2 h. At 03:04 UTC, radar echoes with reflectivity values between 10 and 20 dBZ began to appear in the layer between 2 and 4 km. The first appearance of enhanced radar reflectivity (03:04 UTC) occurred 18 min after the AgI aerosols were released at 02:46 UTC (Figure 5), which roughly represented how long the precipitation particles needed to grow to be large enough for the growth to be discerned by the radar. After 03:10 UTC, the base of the enhanced reflectivity started to descend as the particles grew and fell. The seeding signature reached the surface approximately 40 min after seeding, with a reflectivity value between 20 and 25 dBZ. The tops of the radar echoes above the seeding tracks at a height of 6 km seen in Figures 4d and 4f were caused by the radar beam width, where a strong echo expands with the radar beam pattern (Atlas et al., 1963).

When the seeded clouds moved with the prevailing wind, they were extended not only in the vertical direction but also in the horizontal direction. Rosenfeld, Yu, and Dai (2005) calculated that the fall speed of cloud ice particles from the cloud top after seeding is 0.4 m s^{-1} . The fall speed curve of ice crystals measured by Nakaya and Terada (1935) indicates that the fall speed of pure ice crystals is less than 1 m s^{-1} .

The reflectivity range of 20–25 dBZ expanded approximately 1,000 m downward from 03:04 UTC to 03:33 UTC. Based on this, it is estimated that the hydrometeors fall speed was approximately 1.7 m s^{-1} . Therefore, it is possible that the hydrometeors above the melting level were composed of aggregates and graupels. The location of the Chunhua station was such that the descending reflectivity had just reached the surface when the seeding track passed over it. Therefore, the largest hydrometeors, which fell the fastest, were conspicuously large. The enhanced precipitation reached the surface further downwind of Chunhua station. The largest raindrops of the seeding track captured by the Chunhua station disdrometer reached a



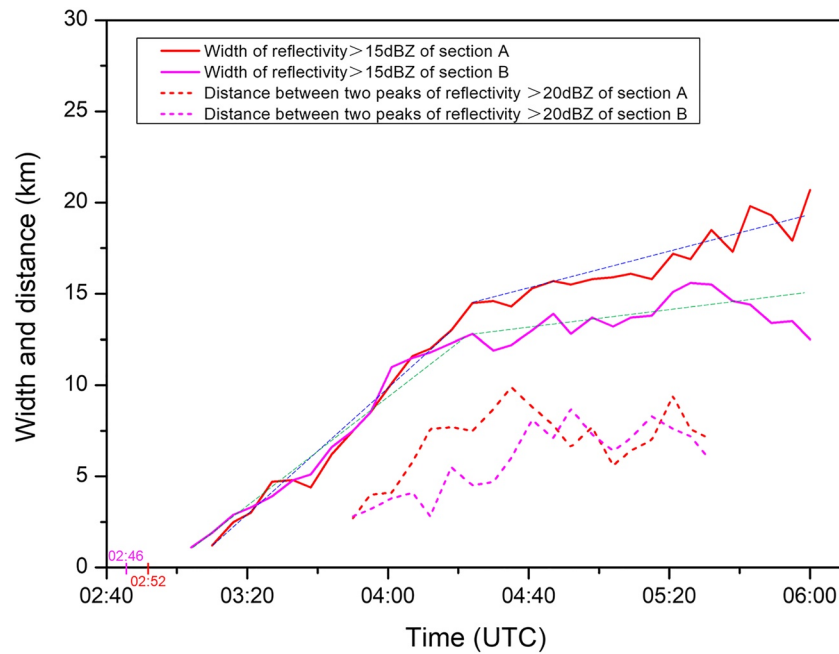


Figure 5. The temporal variation of the widths of the radar seeding tracks. The width is defined by composite reflectivity greater than 15 dBZ across sections (A and B) in Movie S2, marked with solid red and violet lines, respectively. The approximation to slopes is given by the blue broken lines, with an initial expansion rate of 1.4 m s^{-1} which moderated to 0.3 m s^{-1} after 04:25 UTC. The broken lines show the distance between their two reflectivity peaks that exceeded 20 dBZ for part of the time. The seeding time of sections A and B were 02:52 UTC and 02:46 UTC, respectively, as denoted on the abscissa. The time when the seeding lines of cross sections A and B first appeared on radar was 03:10 and 03:04 UTC, respectively.

diameter of 2.75 mm, whereas they reached a diameter of 1 mm outside the track. These hydrometeors fall speeds were much larger than the calculations above based on the descent rate of the reflectivity core. The site of the Tongchuan station was 100 min farther downwind of the Chunhua station. During that time, the seeding signature expanded, weakened, and diffused to the point that there was no clear separation of seeded and unseeded rainfall at the surface, where the rainfall was already very light.

2.2. Seeding Track Observed by Satellite

The signature of cloud seeding was captured not only by the radars but also by the MODIS images onboard the TERRA satellite and visible and infrared radiometer (VIRR) images on the FengYun-3C (FY-3C) satellite. The data utilized were from the TERRA satellite MOD021KM at 03:19 UTC and the FY-3C satellite VIRR L1 1000M at 03:30 UTC on March 19, 2017.

The methodology of satellite retrieval proposed by Rosenfeld and Lensky (1998) was used to retrieve cloud microphysical properties. The “day microphysical color” scheme was used to identify the seeding signature. It assigned a reflectance of 0.6-, 1.6-, and 3.7- μm reflectance and 11- μm brightness temperature to the colors of red, green, and blue, respectively, to form the composited RGB images. The colors of this scheme enabled the qualitative representation of the cloud microstructure. Yellow represents supercooled clouds with small droplets, orange represents supercooled water clouds with medium droplets, and red represents ice clouds

Figure 4. Composite radar reflectivity at the Jinghe radar station (red star, 108.97°E, 34.45°N, 410 m above sea level) at (a) 02:59 UTC, (c) 03:16 UTC, (e) 03:27 UTC, (g) 04:47 UTC, and (i) 05:49 UTC on March 19, 2017. In (a, c, e, g, and i), the cloud-seeding signature observed by radar is marked by a gray rectangular box. The seeding tracks are shown with blue dashed lines. The arrowed orange solid line (the length of 85.2 km) shows the path of cloud motion aligned with the wind over the Chunhua station (red triangle, 108.55°E, 34.83°N). The radar reflectivity in the vertical section (the vertical section along the arrowed orange line was roughly to the northeast) through Chunhua station overlying a part of the Loess Plateau (terrain is gray shaded) in (b, d, f, h, and j). The red and black triangles represent the PARSIVEL rain disdrometer located at the Chunhua and Tongchuan stations (109.08°E, 35.06°N), respectively.

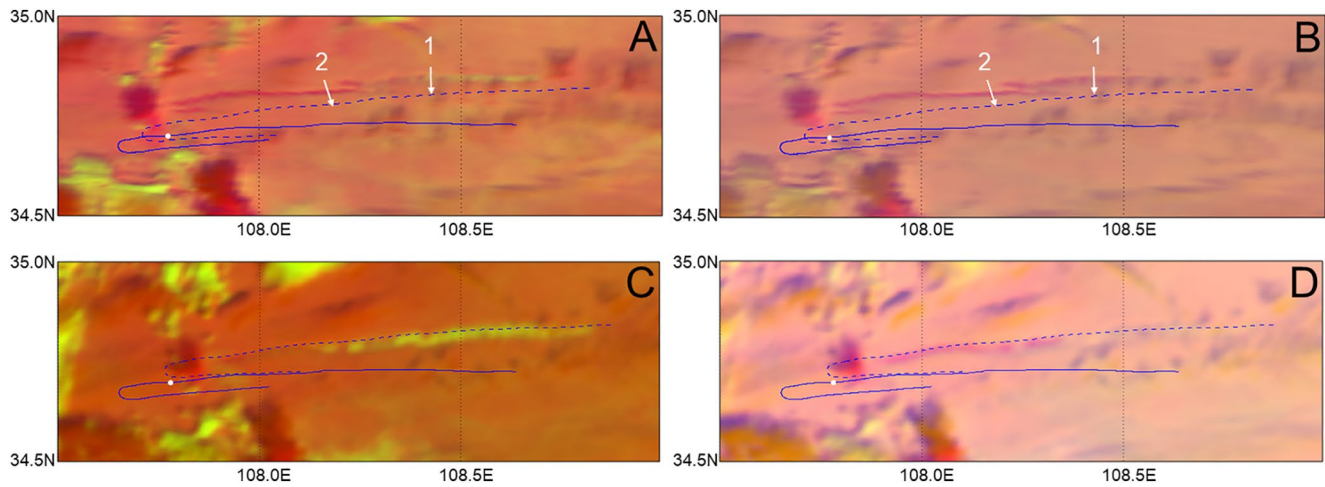


Figure 6. The RGB microphysical composite image from TERRA/MODIS at 03:19 UTC (a and b) and FY3-C at 03:30 UTC (c and d) on March 19, 2017. The RGB microphysical composite images are composed of red (R) for the 0.6- μm visible reflectance, green (G) for the 3.7- μm reflectance in (a and c) and the 1.6- μm reflectance in (b and d), and blue (B) for the inverse of 11- μm brightness temperature (T_{11}). The ice cloud is represented by red, the water cloud with small drops is represented by yellow, and the water cloud with medium sized drops is represented by orange. The seeding track shifted to the time of the satellite overpass is marked by the blue dashed line. The discontinuities of the cloud trace in (a and b) are artifacts caused by the bowtie effect of the MODIS data near the edge of the swath. It also contributed to the mismatch between the aircraft seeding track and shifted seeding track in (a and b). The white lines mark the locations of the cross sections in Figure 7.

(Rosenfeld & Lensky, 1998; Rosenfeld, Liu, et al., 2014). Because the measured 1.6 μm radiation came from clouds deeper than 3.7 μm (Rosenfeld, Cattani, et al., 2004), the RGB composed of reflectances at 3.7 μm (RGB 3.7, Figures 6a and 6c) and at 1.6 μm (RGB 1.6, Figures 6b and 6d) was set to display the cloud microstructures at different depths within the cloud.

The microphysical properties of the seeded cloud and its surroundings were revealed by the TERRA satellite at 03:19 UTC (Figures 6a and 6b) and the FY-3C satellite at 03:30 UTC (Figures 6c and 6d). By using a similar method as in Rosenfeld, Yu, and Dai (2005), these composite images display the cloud top microstructure, with an evident contrast between the flat-top background supercooled layer clouds and the glaciated clouds in the seeded track. The glaciated line marks the seeding track, which appears conspicuously in deeper red, embedded in the ambient supercooled layer clouds in lighter orange colors. The seeding track on the satellite image terminated slightly east of the western edge of the seeder aircraft track because the aircraft descended below the cloud top toward the west end of the leg (Figure 1).

The satellite seeding signature in the form of a glaciated line appeared not later than 15 min after seeding, shortly followed by the appearance of a radar seeding track. The glaciated track was apparent by the strong absorption of solar radiation at 1.6 and 3.7 μm by the ice compared to the adjacent supercooled water cloud. This strong absorption by the ice was depicted in red in the RGB color scheme. The ice absorption of solar radiation is evidenced by the black and green lines of the cross section shown in Figure 7b.

The falling ice crystals produced a trench in the cloud, which induced the warming of cloud tops by nearly 1°C (Figure 7), similar to what was observed in the case documented by Rosenfeld, Yu, and Dai (2005). Approximately 30 min after seeding began, new water clouds with small droplets formed in the cloud trench that were formed by the precipitation of the glaciated cloud particles. These clouds are evidenced by their small cloud drop effective radius, which are shown with a yellow filling in the RGB composite at 3.7 μm , as shown in Figures 6a and 6c. Figure 7 shows the filling of the trench with clouds by the enhanced 3.7- μm reflectance represented by the green line in panel a compared to the reduced 3.7- μm reflectance within the cloud-free channel shown in panel b. The water cloud filling of the seeded trench propagates westward with time following the aging of the seeding track, as evidenced by the comparison of Figure 6c to Figure 6a, which is later by 15 min. The same phenomenon was already documented previously by Rosenfeld, Yu, and Dai (2005). They ascribed it to latent heat release as the glaciation advances downward with the falling ice hydrometeors. The warmed air rose to the cloud trench left by the falling ice particles and formed a new

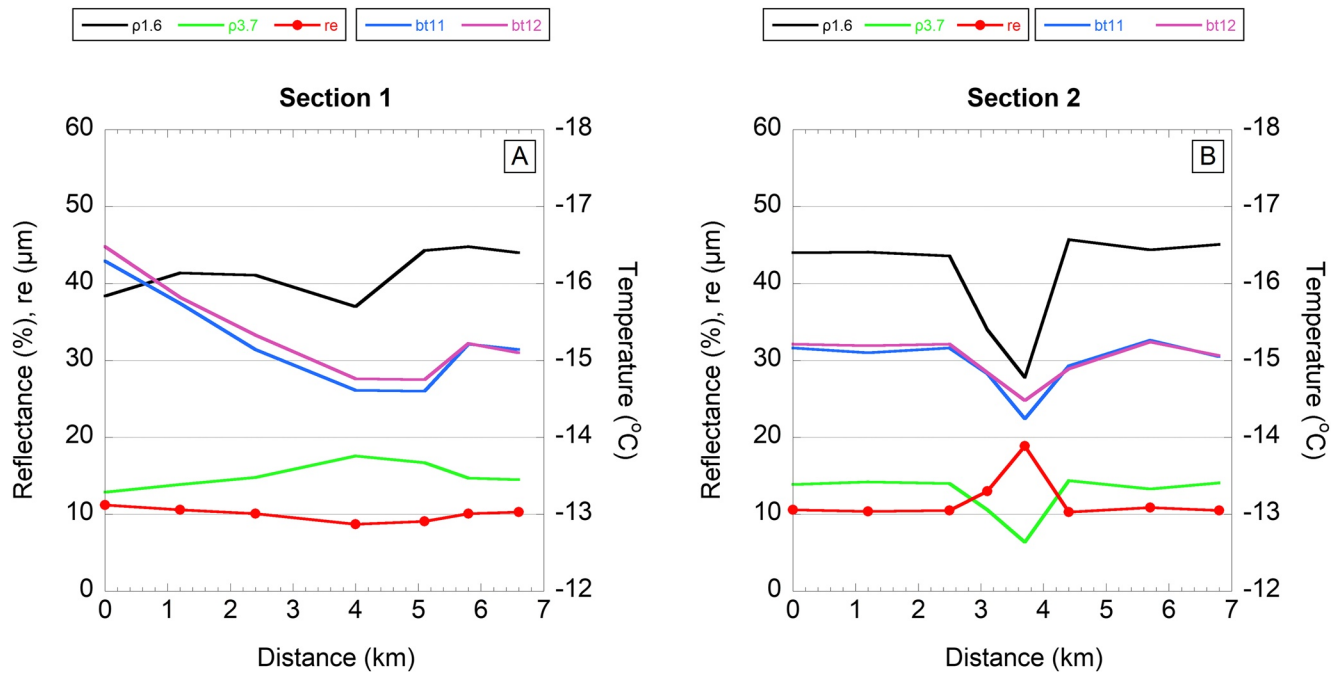


Figure 7. Microphysical properties of the seeding track and its surrounding clouds for two cross sections (marked with white numbers in Figure 6). The 1.6- and 3.7- μm reflectances are shown as black and green lines, respectively. The indicated effective radius (r_e) is red. The 11- and 12- μm brightness temperatures are shown in blue and purple, respectively. The glaciated seeding track (b) is evident with a reduced solar reflectance due to ice absorption and a 1 $^{\circ}\text{C}$ increase in the cloud top temperature due to the collapsed glaciated cloud tops. The formation of new water clouds within the seeded cloud trench (a) is evidenced by the increased solar reflectance and decreased r_e at 3.7 μm . The cold cloud tops on the left part of the cross section (a) belong to a separate upper layer.

supercooled water cloud within the trench, which is shown as the yellow filling of the seeding track in Figures 6a and 6c. The rising air diverged under the inversion and brought the ice nuclei to the walls of the trench and seeded them, which led to the expansion of the seeding track as occurs in the case of punch hole clouds (Heymsfield et al., 2011). The newly formed precipitation on both sides of the expanding seeding track produced two reflectivity peaks. Figure 5 displayed the distance between the two peaks on two parallel cross sections on the left panel in Movie S2 from 02:59 UTC to 06:06 UTC. A conceptual model of the formation of the seeding trench and its filling with water clouds is illustrated in Figure 8.

An alternative explanation might be that the new formation of water clouds in the trench was due to the gentle orographic uplift of the air mass, including the air in the trenches. While possible, it is unlikely to be the main reason because cloud filling is a transient phenomenon that occurs with a lag of ~ 30 min after seeding and clears after up to an additional 30 min later (Rosenfeld, Yu, & Dai, 2005), likely due to the dissipation of the latent heat. The westward propagation of the cloud filling evident between Figures 6a and 6c further supports this hypothesis.

2.3. Surface Precipitation Measurements

Based on radar analyses, the seeding line of composite radar reflectivity > 15 dBZ passed over the Chunhua station between 03:25 and 03:35 UTC (Figure 9a and Movie S1). The three periods/stages of seeding, namely Preseed, Seed, and Postseed, are 03:15–03:24, 03:25–03:35, and 03:36–03:45 UTC, respectively, for the Chunhua station. The passage time of the seeding line with composite reflectivity > 15 dBZ over the Chunhua station was 11 min (Figures 9a and 9c). At 03:30 UTC, the composite reflectivity over Chunhua station reached the maximum of 26 dBZ (Figure 9c). One minute later, the reflectivity calculated from PARSIVEL data reached the maximum of 22.7 dBZ, and the maximum of the mean volume drop diameter appeared at the same time. It indicated that there was a short time delay of the raindrop from the height of radar volume scan to be caught by the PARSIVEL caused by the height difference.

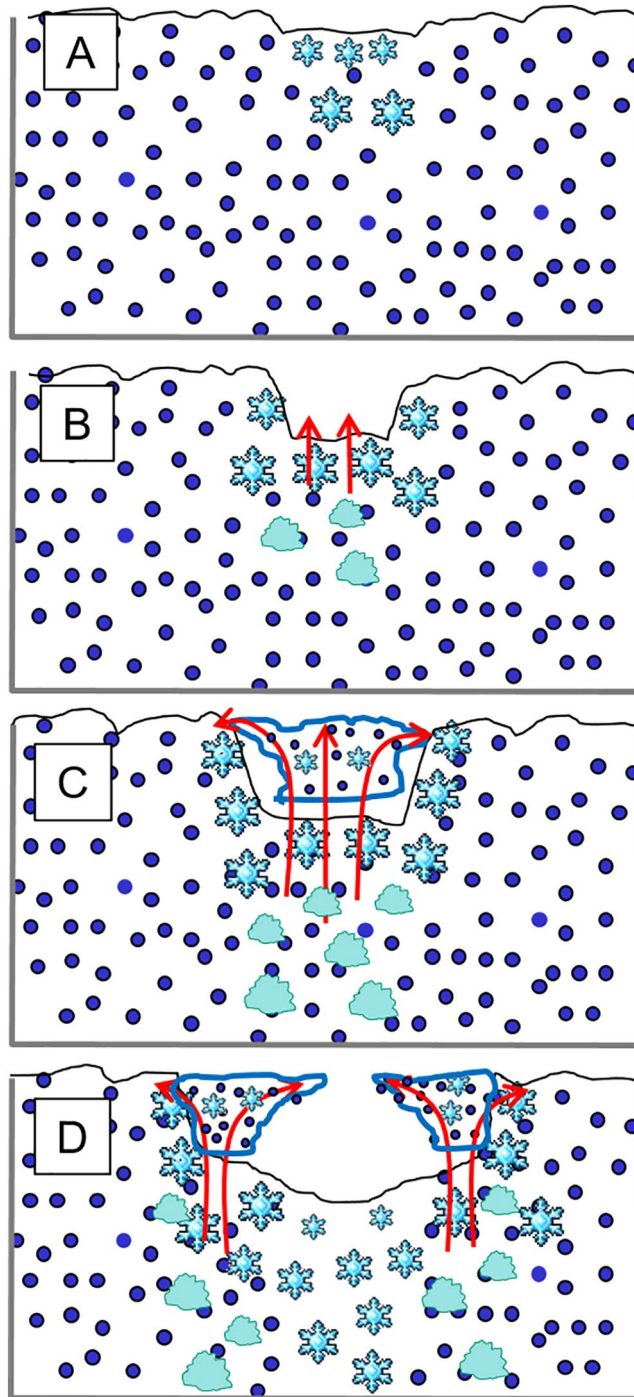
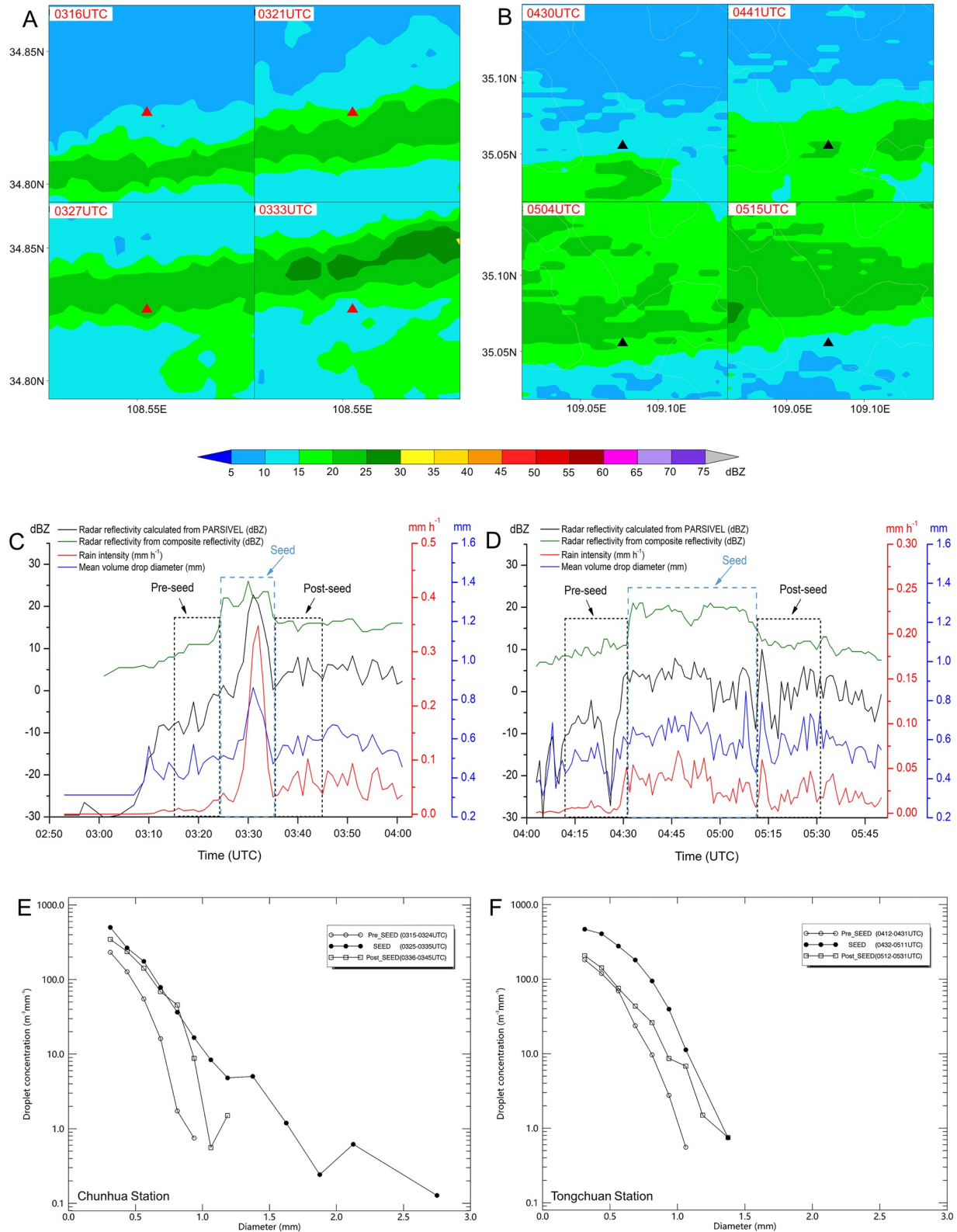


Figure 8. A conceptual model of the formation of the glaciated seeding track, the trench, and its filling with water clouds. The seeding creates a large number of small ice crystals that grow at the expense of supercooled water drops and falls (a). The precipitation of the ice crystal from the cloud top leaves a glaciated trench in the cloud. The crystals grow as they fall, rime and aggregate, and some of them transition into graupels, which fall through the cloud column (b). The latent heat of freezing causes the air to rise and fill the trench with new water clouds, which glaciate later. The rising air keeps the seeding at walls of the trench and expands the seeding track (c). The cloud at the center of the seeding line is completely glaciated so no new latent heat of freezing is released, leading to the dissipation of the cloud above the channel. The lateral mixing of the remaining IN keeps spreading the glaciation sideways, widening the glaciated seeding track, and keeps releasing additional latent heat on the expanding edges, in a similar mechanism documented for “punch hole” clouds (Heymsfield et al., 2011). The released latent heat can lead to growth of additional clouds near the edge of the widening trench (d).



The 0.02-mm surface accumulation at the Chunhua station was likely related to the change in raindrop diameter, which sharply increased from 1.0 to 2.75 mm (Figure 9e) over a very short time after cloud seeding. There was almost no accumulated precipitation recorded before 03:28 UTC and after 03:34 UTC. A total of only 0.02 mm accumulated, with a maximum and mean rates of approximately 0.35 and 0.19 mm h⁻¹, respectively, during the 6-min period just after the seeded cloud line passed over the disdrometer. However, according to the vertical radar cross sections, the descending seeded precipitation shaft barely reached the surface when the seeding track passed over the Chunhua station. Therefore, the largest drops were preferably precipitated, and rain enhancement at the ground was not fully realized at the Chunhua station but rather some distance farther downwind.

Although the accumulated precipitation of 0.02 mm is very small, based on the analysis of radar reflectivity and disdrometer data, we concluded that the light precipitation (0.02 mm) observed by the Chunhua station disdrometer could be unambiguously attributed to cloud seeding. The raindrop spectrum obtained by the Chunhua station disdrometer shown in Figure 9e might have been the first raindrop spectrum image of precipitation generated by cloud seeding.

As the lines propagated downwind, the seeding line of composite reflectivity >15 dBZ passed over the Tongchuan station between 04:32 and 05:11 UTC (Figure 9b). The Preseed, Seed, and Postseed periods were 04:12–04:31, 04:32–05:11, and 05:12–05:31 UTC for Tongchuan station, respectively. The seeding line split into a double band when it passed over Tongchuan station (Figure 9b). Correspondingly, there was a transition from a single peak reflectivity to two peaks of reflectivity, as seen in Figure 9d and in the right panels in Movie S2. Compared with the passage time of the seeding line with composite reflectivity >15 dBZ over the Chunhua station, the passage time over the Tongchuan station increased to 40 min. The big difference between the composite reflectivity and reflectivity calculated from PARSIVEL data is attributed to the large vertical distance between radar observation and disdrometer. The raindrop spectrum measured on the surface at this station (Figure 9f) showed that cloud seeding had a positive contribution to the precipitation enhancement (Figure 9f).

3. Discussions and Conclusions

This study provided documentation of the evolution of a glaciogenic seeding track in supercooled layer clouds over central China. Observations from satellite, ground-based weather radar, and laser raindrop disdrometers were presented that additively provide the spatial and temporal evolution of the cloud-seeding line and the strongest evidence available so far for the mechanisms by which glaciogenic seeding can affect precipitation-forming processes in China. The combined observations offer physical evidence for the processes leading from cloud seeding to additional rainfall reaching the ground.

A seeding airplane released AgI aerosols from 02:41 to 03:14 UTC. The radar detected a seeding line of enhanced reflectivity within 18 min after seeding began. The seeding signature, as evidenced by enhanced radar reflectivity, moved with the prevailing wind at the seeding level and expanded. The reflectivity seeding signature increased to 25–30 dBZ appeared in 46 min, and its length was then 84 km and its width was 5 km. The width reached 15 km by 126 min after cloud seeding began. The seeding signature disappeared 234 min after cloud seeding began. The expansion rate of the seeding line/area was at approximately ~1.4 and ~0.3 m s⁻¹ before and after 04:25 UTC as it moved to the northeast. The seeding altitude was mostly 4 km and descended to 3 km near the end. The radar echo of the seeding signature was initially observed at an altitude of 3,700 m, where the temperature was near –15°C.

The analysis of the data measured by the MODIS satellite overpass at 03:19 UTC on March 19, 2017, captured the seeding line after seeding began. A simultaneous radar observation took place at 03:16 UTC. The

Figure 9. The seeding signatures at the rain gauge sites. Composite radar reflectivity around the Chunhua station (red triangle, a) and Tongchuan station (black triangle, b) during the passage of seeding line. The temporal variations of rain properties in Chunhua (c) and Tongchuan (d) are shown as green lines for the radar composite reflectivity (dBZ) from the radar above the rain gauge sites, and as black lines for reflectivity calculated from PARSIVEL. Rain intensity (mm h⁻¹) and mean volume drop diameter (mm) are shown by the red and blue lines, respectively. (e and f) The seeded versus preseeded and postseeded drop size distributions are shown for Chunhua (e) and Tongchuan (f) rain gauges. The times are shown by the rectangles in panels (c and d). PARSIVEL, particle size velocity.

seeding track was embedded in the ambient supercooled layer clouds. The satellite observations at that time (Figures 6a and 6b) showed that the seeding track was a glaciated trench in the clouds caused by the sinking of the glaciated particles at the cloud top. New water clouds with small droplets formed within the seeding track (shown in yellow in Figure 6a). The formation of these clouds implied that air rose within the seeding tracks, likely as a result of the latent heat release of freezing of the seeding track. A similar phenomenon was previously observed by Rosenfeld, Yu, and Dai (2005).

The enhanced radar echo descended and reached the surface 40 min after seeding started as it passed the location of the laser raindrop disdrometers at Chunhua station. The seeding effect was indicated by the disdrometer as a small concentration of abnormally large raindrops (up to 2.75 mm in diameter) compared to those less than 1 mm before and after the passage of the seeding signature. The reflectivity continued to increase and expand further downwind of the measuring site, indicating that the effect on the surface rain rate was probably much larger there than that measured at the Chunhua station disdrometer. It appears that only the largest hydrometeors had sufficient time to reach the ground at the Chunhua station. By the time (100 min after passing Chunhua station) that the seeding track reached the Tongchuan disdrometer, with clearly evident excess surface precipitation rate. This chain of events following the seeding of supercooled layer clouds supports the full microphysical chain of events due to airborne glaciogenic seeding of orographic clouds demonstrated by French et al. (2018).

A conceptual model is presented in Figure 8 and constituted of the following steps:

1. The seed agent initiates ice crystals which glaciate the cloud after ~15 min and produces ice hydrometeors detectable by radar (>20 dBZ) shortly (few minutes) after that.
2. The aggregated and rimed hydrometeors precipitate and leave a visible channel at cloud top.
3. While descending, the ice particles rime the cloud water at lower levels and grow while releasing additional latent heat of freezing.
4. The warmed air rises into the channel and fills it with a newly formed cloud with small supercooled water droplets.
5. The rising air which contains ice nuclei and small ice crystals diverges under the inversion which marks the top of the general field of clouds and impinges and mixes with the ambient supercooled layer clouds, thereby expanding the seeding track at a two sided rate of $\sim 1.4 \text{ m s}^{-1}$.
6. The expansion to the ambient clouds generates fresh ice hydrometeors, which form a widening double peak band of precipitation intensity.
7. After ~90 min, the expansion rate decreases from ~ 1.4 to $\sim 0.3 \text{ m s}^{-1}$, probably due to exhaustion of the ice nuclei available to seeding additional clouds at the periphery.

The added surface rainfall was probably small. However, the results demonstrate that adding ice nuclei can transfer a cloud on the verge of precipitating or lightly precipitating to precipitate. This has importance to climate studies because of its implications for cloud lifetime and radiative properties, so it may be related to the effect of changes in the ice nuclei concentration on climate.

In view of these findings and their importance, it is necessary to utilize cloud microphysical observation equipment and design thorough scientific and field experiments in future studies. Such studies will enable a more comprehensive understanding of artificial enhancement precipitation operations to better conduct scientific operations and improve program effectiveness.

Data Availability Statement

Composite radar reflectivity and sounding data were obtained from China Meteorological Data Service Center (CMDC). Composite reflectivity data used can be downloaded publicly online (<http://data.cma.cn/en/?r=data/detail&dataCode=J.0012.0003>). The sounding data used in this study are archived online (<http://data.cma.cn/en/?r=data/detail&dataCode=B.0011.0001C>). The FY-3C/VIRR data were obtained from National Satellite Meteorological Center (NSMC) of China Meteorological Administration (<http://satellite.nsmc.org.cn/portalsite/default.aspx>). The TERRA/MODIS data were obtained from Atmosphere Archive & Distribution System (LAADS) Distributed Active Archive Center (DAAC) (<https://ladsweb.modaps.eosdis.nasa.gov/search/>).

References

- Atlas, D., Browning, K. A., Donaldson, R. J., & Sweeney, H. J. (1963). Automatic digital radar reflectivity analysis of a tornadic storm. *Journal of Applied Meteorology*, 2(5), 574–581.
- Chu, X., Geerts, B., Xue, L., & Pokharel, B. (2017). A case study of cloud radar observations and large-eddy simulations of a shallow stratiform orographic cloud, and the impact of glaciogenic seeding. *Journal of Applied Meteorology and Climatology*, 56(5), 1285–1304. <https://doi.org/10.1175/JAMC-D-16-0364.1>
- Chu, X., Geerts, B., Xue, L., & Rasmussen, R. (2016). Large-eddy simulations of the impact of ground-based glaciogenic seeding on shallow orographic convection: A case study. *Journal of Applied Meteorology and Climatology*, 56(1), 69–84. <https://doi.org/10.1175/JAMC-D-16-0191.1>
- Chu, X., Xue, L., Geerts, B., Rasmussen, R., & Breed, D. (2014). A case study of radar observations and WRF LES simulations of the impact of ground-based glaciogenic seeding on orographic clouds and precipitation. Part I: Observations and model validations. *Journal of Applied Meteorology and Climatology*, 53(10), 2264–2286. <https://doi.org/10.1175/JAMC-D-14-0017.1>
- Dong, X., Zhao, C., Yang, Y., Wang, Y., Sun, Y., & Fan, R. (2020). Distinct change of supercooled liquid cloud properties by aerosols from an aircraft-based seeding experiment. *Earth and Space Science*, 7(8), e2020EA001196. <https://doi.org/10.1029/2020EA001196>
- Flossmann, A. I., Manton, M., Abshaev, A., Bruinjtjes, R., Murakami, M., Prabhakaran, T., & Yao, Z. (2018). *Peer review report on global precipitation enhancement activities* (Research Report). World Meteorological Organization. Retrieved from <https://hal.uca.fr/hal-01917801>
- French, J. R., Friedrich, K., Tessoroff, S. A., Rauber, R. M., Geerts, B., Rasmussen, R. M., et al. (2018). Precipitation formation from orographic cloud seeding. *Proceedings of the National Academy of Sciences*, 115(6), 1168–1173. <https://doi.org/10.1073/pnas.1716995115>
- Friedrich, K., Ikeda, K., Tessoroff, S. A., French, J. R., Rauber, R. M., Geerts, B., et al. (2020). Quantifying snowfall from orographic cloud seeding. *Proceedings of the National Academy of Sciences*, 117(10), 5190–5195. <https://doi.org/10.1073/pnas.1917204117>
- Gabriel, K. R. (1999). Ratio statistics for randomized experiments in precipitation stimulation. *Journal of Applied Meteorology*, 38(3), 290–301. [https://doi.org/10.1175/1520-0450\(1999\)038<0290:RSFREI>2.0.CO;2](https://doi.org/10.1175/1520-0450(1999)038<0290:RSFREI>2.0.CO;2)
- Geerts, B., Miao, Q., Yang, Y., Rasmussen, R., & Breed, D. (2010). An airborne profiling radar study of the impact of glaciogenic cloud seeding on snowfall from winter orographic clouds. *Journal of the Atmospheric Sciences*, 67(10), 3286–3302. <https://doi.org/10.1175/2010jas3496.1>
- Gultepe, I., Kuhn, T., Pavlonis, M., Calvert, C., Gurka, J., Heymsfield, A. J., et al. (2014). Ice fog in Arctic during FRAM-Ice Fog project: Aviation and nowcasting applications. *Bulletin of the American Meteorological Society*, 95(2), 211–226. <https://doi.org/10.1175/bams-d-11-00071.1>
- Heymsfield, A. J., Thompson, G., Morrison, H., Bansemer, A., Rasmussen, R. M., Minnis, P., et al. (2011). Formation and spread of aircraft-induced holes in clouds. *Science*, 333(6038), 77–81. <https://doi.org/10.1126/science.1202851>
- Hobbs, P. V. (1975). The nature of winter clouds and precipitation in the cascade mountains and their modification by artificial seeding. Part III: Case studies of the effects of seeding. *Journal of Applied Meteorology*, 14(5), 819–858. [https://doi.org/10.1175/1520-0450\(1975\)014<0819:TNOWCA>2.0.CO;2](https://doi.org/10.1175/1520-0450(1975)014<0819:TNOWCA>2.0.CO;2)
- Hobbs, P. V., Lyons, J. H., Locatelli, J. D., Biswas, K. R., Radke, L. F., Weiss, R. R., Sr., & Rangno, A. L. (1981). Radar detection of cloud-seeding effects. *Science*, 213(4513), 1250–1252. <https://doi.org/10.1126/science.213.4513.1250>
- Huggins, A. W. (2007). Another wintertime cloud seeding case study with strong evidence of seeding effects. *Journal of Weather Modification*, 39(1), 9–36.
- Langmuir, I. (1961). In G. Suits & H. E. Way (Eds.), *Collected works of Langmuir* (Vols. 10–11). Pergamon Press.
- Löffler-Mang, M., & Joss, J. (2000). An optical disdrometer for measuring size and velocity of hydrometeors. *Journal of Atmospheric and Oceanic Technology*, 17(2), 130–139. [https://doi.org/10.1175/1520-0426\(2000\)017<0130:AODFMS>2.0.CO;2](https://doi.org/10.1175/1520-0426(2000)017<0130:AODFMS>2.0.CO;2)
- Manton, M. J., Warren, L., Kenyon, S. L., Peace, A. D., Bilish, S. P., & Kemsley, K. (2011). A confirmatory snowfall enhancement project in the Snowy Mountains of Australia. Part I: Project design and response variables. *Journal of Applied Meteorology and Climatology*, 50(7), 1432–1447. <https://doi.org/10.1175/2011JAMC2659.1>
- Morrison, A. E., Siems, S. T., & Manton, M. J. (2013). On a natural environment for glaciogenic cloud seeding. *Journal of Applied Meteorology and Climatology*, 52(5), 1097–1104. <https://doi.org/10.1175/JAMC-D-12-0108.1>
- Nakaya, U., & Terada, T., Jr. (1935). Simultaneous observations of the mass, falling velocity and form of individual snow crystals. *Journal of the Faculty of Science, Hokkaido Imperial University. Series 2, Physics*, 1(7), 191–200.
- Platnick, S., Meyer, K. G., King, M. D., Wind, G., Amarasinghe, N., Marchant, B., et al. (2017). The MODIS cloud optical and microphysical products: Collection 6 updates and examples from terra and aqua. *IEEE Transactions on Geoscience and Remote Sensing*, 55(1), 502–525. <https://doi.org/10.1109/TGRS.2016.2610522>
- Pokharel, B., Geerts, B., & Jing, X. (2018). The impact of ground-based glaciogenic seeding on a shallow stratiform cloud over the Sierra Madre in Wyoming: A multi-sensor study of the 3 March 2012 case. *Atmospheric Research*, 214(20), 74–90. <https://doi.org/10.1016/j.atmosres.2018.07.013>
- Pokharel, B., Geerts, B., Jing, X., Friedrich, K., Aikins, J., Breed, D., et al. (2014). The impact of ground-based glaciogenic seeding on clouds and precipitation over mountains: A multi-sensor case study of shallow precipitating orographic cumuli. *Atmospheric Research*, 147–148, 162–182. <https://doi.org/10.1016/j.atmosres.2014.05.014>
- Pokharel, B., Geerts, B., Jing, X., Friedrich, K., Ikeda, K., & Rasmussen, R. (2017). A multi-sensor study of the impact of ground-based glaciogenic seeding on clouds and precipitation over mountains in Wyoming. Part II: Seeding impact analysis. *Atmospheric Research*, 183, 42–57. <https://doi.org/10.1016/j.atmosres.2016.08.018>
- Rasmussen, R. M., Tessoroff, S. A., Xue, L., Weeks, C., Ikeda, K., Landolt, S., et al. (2018). Evaluation of the Wyoming Weather Modification Pilot Project (WWMPP) using two approaches: Traditional statistics and ensemble modeling. *Journal of Applied Meteorology and Climatology*, 57(11), 2639–2660. <https://doi.org/10.1175/JAMC-D-17-0335.1>
- Rauber, R. M., Geerts, B., Xue, L., French, J., Friedrich, K., Rasmussen, R. M., et al. (2019). Wintertime orographic cloud seeding—A review. *Journal of Applied Meteorology and Climatology*, 58(10), 2117–2140. <https://doi.org/10.1175/JAMC-D-18-0341.1>
- Rosenfeld, D. (2000). Suppression of rain and snow by urban and industrial air pollution. *Science*, 287(5459), 1793–1796. <https://doi.org/10.1126/science.287.5459.1793>
- Rosenfeld, D., Cattani, E., Melani, S., & Levizzani, V. (2004). Considerations on daylight operation of 1.6- versus 3.7- μm channel on NOAA and METOP satellites. *Bulletin of the American Meteorological Society*, 85(6), 873–882. <https://doi.org/10.1175/BAMS-85-6-873>
- Rosenfeld, D., & Lensky, I. M. (1998). Satellite-based insights into precipitation formation processes in continental and maritime convective clouds. *Bulletin of the American Meteorological Society*, 79(11), 2457–2476. [https://doi.org/10.1175/1520-0477\(1998\)079<2457:SBIIPF>2.0.CO;2](https://doi.org/10.1175/1520-0477(1998)079<2457:SBIIPF>2.0.CO;2)

Acknowledgments

This work was supported by the National Key R&D Program of China (2016YFA0601704 and 2018YFC1507903), National Natural Science Foundation of China (41627807 and 41575136), Natural Science Basic Research Plan of Shaanxi (2021JQ-966), Key Research and Development Program of Shaanxi (2020SF-429, 2020ZDLSF06-02 and 2021ZDZLGY09-09), Key Laboratory for Cloud Physics of China Meteorological Administration (2020Z007), and Research fund for Weather modification ability construction project of Northwest China (RYSY201905 and RYSY201909). The authors greatly appreciate colleagues of Weather Modification Center of Shaanxi Province for their participation in the rain enhancement operation of aircraft and thank the National Center for Weather Modification for processing radar data system of CPAS.

- Rosenfeld, D., Liu, G., Yu, X., Zhu, Y., Dai, J., Xu, X., & Yue, Z. (2014). High-resolution (375 m) cloud microstructure as seen from the NPP/VIIRS satellite imager. *Atmospheric Chemistry and Physics*, *14*(5), 2479–2496. <https://doi.org/10.5194/acp-14-2479-2014>
- Rosenfeld, D., Yu, X., & Dai, J. (2005). Satellite-retrieved microstructure of AgI seeding tracks in supercooled layer clouds. *Journal of Applied Meteorology*, *44*(6), 760–767. <https://doi.org/10.1175/JAM2225.1>
- Rosenfeld, D., Zhu, Y., Wang, M., Zheng, Y., Goren, T., & Yu, S. (2019). Aerosol-driven droplet concentrations dominate coverage and water of oceanic low-level clouds. *Science*, *363*(6424), eaav0566. <https://doi.org/10.1126/science.aav0566>
- Super, A. B., & Boe, B. A. (1988). Microphysical effects of wintertime cloud seeding with silver iodide over the Rocky Mountains. Part III: Observations over the Grand Mesa, Colorado. *Journal of Applied Meteorology*, *27*(10), 1166–1182. [https://doi.org/10.1175/1520-0450\(1988\)027<1166:MEOOWCS>2.0.CO;2](https://doi.org/10.1175/1520-0450(1988)027<1166:MEOOWCS>2.0.CO;2)
- Super, A. B., Boe, B. A., Holroyd, E. W., & Heimbach, J. A. (1988). Microphysical effects of wintertime cloud seeding with silver iodide over the Rocky Mountains. Part I: Experimental design and instrumentation. *Journal of Applied Meteorology*, *27*(10), 1145–1151. [https://doi.org/10.1175/1520-0450\(1988\)027<1145:MEOOWCS>2.0.CO;2](https://doi.org/10.1175/1520-0450(1988)027<1145:MEOOWCS>2.0.CO;2)
- Xue, L., Chu, X., Rasmussen, R., Breed, D., & Geerts, B. (2016). A case study of radar observations and WRF LES simulations of the impact of ground-based glaciogenic seeding on orographic clouds and precipitation. Part II: AgI dispersion and seeding signals simulated by WRF. *Journal of Applied Meteorology and Climatology*, *55*(2), 445–464. <https://doi.org/10.1175/JAMC-D-15-0115.1>
- Xue, L., Hashimoto, A., Murakami, M., Rasmussen, R., Tessoroff, S. A., Breed, D., et al. (2013). Implementation of a silver iodide cloud-seeding parameterization in WRF. Part I: Model description and idealized 2D sensitivity tests. *Journal of Applied Meteorology and Climatology*, *52*(6), 1433–1457. <https://doi.org/10.1175/JAMC-D-12-0148.1>
- Yue, Z., Rosenfeld, D., Liu, G., Dai, J., Yu, X., Zhu, Y., et al. (2019). Automated Mapping of Convective Clouds (AMCC) thermodynamical, microphysical, and CCN properties from SNPP/VIIRS satellite data. *Journal of Applied Meteorology and Climatology*, *58*(4), 887–902. <https://doi.org/10.1175/JAMC-D-18-0144.1>
- Yu, X., Dai, J., Rosenfeld, D., Lei, H., Xu, X., Fan, P., & Chen, Z. (2005). Comparison of model-predicted transport and diffusion of seeding material with NOAA satellite-observed seeding track in supercooled layer clouds. *Journal of Applied Meteorology*, *44*(6), 749–759. <https://doi.org/10.1175/JAM2224.1>